Correlating Structure and Photocurrent for Composite Semiconducting Nanoparticles with Contrast Variation Small-Angle Neutron Scattering and Photoconductive Atomic Force Microscopy

Jeffrey J. Richards,[†] Curtis L. Whittle,[†] Guozheng Shao,[‡] and Lilo D. Pozzo[†,*]

[†]Department of Chemical Engineering and [‡]Department of Chemistry, University of Washington, Seattle Washington 98195, United States

ABSTRACT Aqueous dispersions of semiconducting nanoparticles have shown promise as a robust and scalable platform for the production of efficient polymer/fullerene active layers in organic photovoltaic applications. Semiconducting nanoparticles are a composite of both an n-type and p-type semiconductor contained within a single nanoparticle. In order to realize efficient organic solar cells from these materials, there is a need to understand how the size and internal distribution of materials within each nanoparticle contributes to photocurrent generation in a nanoparticle-derived device. Therefore, characterizing the internal distribution of conjugated polymer and fullerene within the dispersion is the first step to improving performance. To date, study of polymer/fullerene structure within these nanoparticles has been limited to microscopy techniques of deposited nanoparticles. In this work, we use contrast variation with small-angle neutron scattering to determine the internal distribution of poly(3-hexylthiophene) and [6,6]phenyl-C_{61}-butyric acid methyl ester inside the composite nanoparticles as a function of formulation while in dispersion. On the basis of these measurements, we connect the formulation of these nanoparticles with their internal structure. Using electrostatic deposited monolayers of these nanoparticles, we characterize intrinsic charge generation using photoconductive atomic force microscopy and correlate this with structures determined from small-angle neutron scattering measurements. These techniques combined show that the best performing composite nanoparticles are those that have a uniform distribution of conjugated polymer and fullerene throughout the nanoparticle volume such that electrons and holes are easily transported out of the particle.

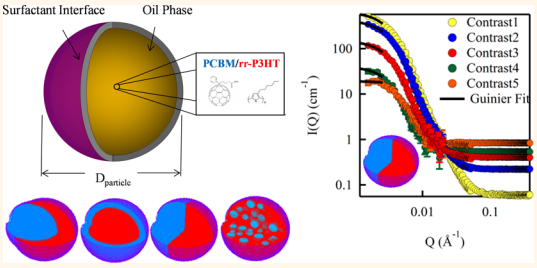

KEYWORDS: composite · nanoparticle · small-angle neutron scattering · contrast variation · organic solar cell · photoconductive AFM

Composite thin films of conjugated polymers and fullerenes comprise the active layer of efficient polymer solar cells. It is within this layer that light is absorbed, photogenerated excitons are dissociated into free carriers, and free carriers are transported to the electrodes.[1−3] In the current paradigm of solution phase processing, these composites are produced using a combination of solvent casting and thermal annealing. This process results in phase-separated polymer and fullerene domains within the active layer. While many other factors can influence photovoltaic performance, the size of these domains and their intrinsic interconnectivity have significant influence on the rate of exciton dissociation and efficiency of carrier extraction.[4] While the past few years have seen enhanced device performance, driven primarily by developments in synthesis of low band gap conjugated polymers, there remains significant process-performance dependencies for thin-film composites processed from organic solvents. Processing parameters, such as annealing temperature,

* Address correspondence to dpozzo@u.washington.edu.

Received for review November 14, 2013 and accepted April 7, 2014.

Published online April 07, 2014
10.1021/nn405914g

blend ratio, film thickness, and material purity, all must be optimized to achieve the best performance given a set of materials. Additionally, this optimization is dependent on the thermal history and drying rate.[5] Therefore, each method requires a different recipe to achieve the best efficiency. This fact compromises the promise of polymer solar cells as an inexpensive alternative to inorganic devices because gains achieved at laboratory scales do not always translate to manufacturing processes for large-area devices with flexible substrates.

It has been proposed that the deposition of semiconducting nanoparticles (SNPs) that are a composite of conjugated polymers and fullerenes could help alleviate this problem.[6,7] This approach offers many potential advantages over organic solvent-based thin-film processing. In the dispersed phase, the distribution of conjugated polymer and fullerene can be fixed before the deposition process. Therefore, the development of microscale morphology can be decoupled from the specific coating operation. In this way, it is possible to optimize the intrinsic characteristics of a given nanoparticle formulation for the best photovoltaic performance and then optimize the coating process to yield a set of extrinsic film properties. This is highly desirable for large-scale coating operations as it affords flexibility in the formulation of these dispersions without influencing or changing the internal structure of the dispersed phase material. Another significant advantage of this approach is that composite nanoparticles can be processed from aqueous dispersions instead of harmful organic solvents. This effectively eliminates the evolution of organic solvent during the coating process, greatly reducing environmental impact and lowering the cost of large-scale coating operations.

Unlike polymer/fullerene active layers that are continuous, SNPs are discrete. Therefore, exciton generation, dissociation, and carrier transport all take place within the volume of a single SNP. The efficiency of this process is directly determined by the distribution of polymer and fullerene within the particle. Within the volume of each nanoparticle, light is absorbed, generating excitons. Those excitons must reach a polymer/fullerene interface where they dissociate into electrons and holes, which must be subsequently transported out of the nanoparticle. Therefore, the optimal morphology within each nanoparticle should be similar to that observed in efficient thin-film active layers cast from solution phase. However, this is not the only consideration important for active layers composed of SNPs. Because of the discrete nature of SNPs, photovoltaic action in a functioning device will depend on ensemble characteristics of particles acting within the composite film. In this way, the performance of a device composed of many SNPs will depend not only on the intrinsic properties of each nanoparticle but also on the spatial distribution of particles within the film. Unavoidable void space due to particle packing, surfactant embedded within the film during the deposition process, and, in the case of multilayers of SNPs, potential bottlenecks caused by interparticle charge transport will all influence the charge transport of SNP-derived active layers.

A number of groups, including ours, are pursuing research aimed at producing efficient photoactive layers from SNPs.[8,9] To date, however, most efforts have focused on optimizing the extrinsic elements of device fabrication, such as annealing temperature, film thickness, and particle composition. Little effort has been made toward characterizing and improving the intrinsic morphology of SNPs despite its critical importance in determining overall device performance.[10] SNPs can be made through a variety of different methods, and each is likely to result in different distributions of polymer/fullerene domains within the particle volume.[11] In order to engineer efficient photovoltaic devices from SNPs, an effective strategy would be to first develop an understanding of how the structure and the distribution of conjugated polymer and fullerene domains inside SNPs correlates to their photovoltaic performance. Then, engineer the deposition process in order to distribute the particles into a thin film such that the overall composite's performance is optimized.

In order to do this, there is a need for techniques that can reconstruct the three-dimensional distribution of material within the nanoparticles and methods that can measure performance metrics from single particles. Recent efforts using X-ray microscopy to directly image SNPs composed of poly(3-hexylthiophene) (P3HT) and [6,6]phenyl-C_{61}-butyric acid methyl ester (PCBM) have proven effective to identify fullerene-rich regions internal to the particle's volume. This approach is feasible due to a difference in the absorption cross section of soft X-rays between P3HT and PCBM. On the basis of these results, the authors determined that P3HT preferentially segregates to the shell of their nanoparticles, forming a core−shell structure. While this is a powerful method for SNP characterization, microscopy techniques are limited to characterizing a small number of particles and cannot be applied in the dispersed phase. Therefore, there can sometimes be uncertainty on how sample preparation and coating may affect morphology. Finally, the extraction of quantitative information is complicated by the projection of three-dimensional information onto a two-dimensional image.

Often, small-angle neutron scattering (SANS) is used as an alternative or complementary method to microscopy in order to characterize the structure of many dispersed materials.[12] SANS is a nondestructive technique that simultaneously probes a large sample volume, averaging large numbers of particles, to characterize the average structure of the dispersion.

By using contrast variation (*i.e.*, varying the H_2O/D_2O content of the dispersed phase), the internal structure of composite nanoparticles can be revealed without changing their chemical environment.[13,14] Further, when materials do not have sufficient electron/X-ray contrast for microscopy, partial or full deuteration of one component can be used to highlight the internal structure of the nanoparticles without changing the chemical identity of either component. In addition to these benefits, the use of appropriate structural models can yield quantitative values related to physical parameters including nanoparticle size, shape, composition, and phase-separation length scale of the components.

In this work, we demonstrate that it is possible to use contrast variation SANS to uniquely identify the internal structure of composite nanoparticles derived from poly(3-hexylthiophene) and [6,6]phenyl-C_{61}-butyric acid methyl ester. We also show that, by manipulating the processing conditions of these particles, it is possible to form a variety of different structures beyond core−shell particles. Other structures include eccentric particles and uniformly distributed heteroaggregates. This is contrary to studies that have recently proposed that core−shell structures are inherent to the production of SNPs from conjugated polymers and fullerenes.[15] In addition to structural characterization, our work shows that particles with the same overall composition, but different structures, give rise to different photovoltaic performance using photoconductive AFM measurements. Further, we demonstrate the electrostatic assembly of SNPs onto PEDOT:PSS-coated ITO substrates. This work established a strong foundation using a variety of techniques to address the issue of engineering efficient photovoltaic active layers from SNPs.

RESULTS

SNPs formed through the removal of solvent from an emulsion are expected to exhibit a wide range of internal morphologies depending on the method of production.[16] As elucidated by Loxley *et al.*, when oil is removed from an emulsion, low volatility components segregate relative to one another to minimize unfavorable interfacial interactions. Therefore, it is expected that solid polymer and fullerene phases formed within the droplets can migrate inside the droplet while it is still fluid. As the drop volume shrinks, the preference of the solvent for the oil−water interface and the solubility of each component in that particular solvent will ultimately determine the internal distribution of the components in the particle when all of the oil is removed. For such systems, a number of possible structures could form: core−shell particles, occluded, eccentric, and uniform. Nanoparticles with identical composition but variable structure are depicted in Figure 1 along with simulated scattering profiles at different contrasts. The corresponding Stuhrmann plots are also shown for each model as constructed from corresponding fits of eq 2. The fitting procedure used is outlined in the Supporting Information. For simple comparison, R_g^2 values are normalized by dividing by R_c^2 and the *x*-axis is normalized by multiplying by ρ_m. This is a convenient way to represent the Stuhrmann plot because it eliminates effects due to variations in size and average contrast. This allows for direct comparison of particles that can have different sizes, structures, and average scattering length densities.

As is evident from Figure 1, the Stuhrmann plots for particles that have a diverse range of internal heterogeneity are very different. This key observation allows for simple identification of structures without assuming a specific structural model *a priori*. As seen in Figure 1, axisymmetric particles (*e.g.*, core−shell) show a linear dependence of R_g *versus* $1/\Delta\rho$ due to the fact that the center of mass of the particle directly corresponds to the center of distribution of scattering length density. Only non-axisymmetric particles like the eccentric particles, where the center of mass of the particle does not correspond to the center of scattering length density, show a nonzero β value. This results in a quadratic dependence of R_g^2 on $1/\Delta\rho$. For the two core−shell particles, β is zero and the radial distribution of higher and lower scattering length density domains determines the sign and value of α. Based on simulated structures in Figure 1, if P3HT (*i.e.*, the lower contrast component) is enriched in the core of the nanoparticle, then α is positive. In contrast, if P3HT is enriched in the shell of the nanoparticle, then α is negative. It is expected that a particle with a uniform distribution of material in its volume will have zero α and β. This should be the case for both the uniform nanoparticle, which lacks any phase separation, and for the occluded nanoparticle where small nuclei are formed in the interior but they are uniformly distributed. Yet, both examples show a very small but finite slope. This is a result of the explicit inclusion of surfactant shell in the simulated models. Thus, all of the particles will show at least a very small amount of heterogeneity. Still, the value of α is very small because the contribution of the surfactant to the overall nanoparticle size is also small.

Four different dispersions were prepared with different methods and measured at five different contrasts in order to obtain similar Stuhrmann plots from a diverse set of nanoparticle formulations (Figure 2). The particles all have a constant 1:1 P3HT to fullerene weight ratio and a similar average particle size. Different particles show varying degrees of dependence on the radius of gyration on the changing contrast of the aqueous phase. The sample in Figure 2a was prepared by dissolving P3HT and PCBM in chloroform. Based on the Stuhrmann plot, this formulation results in a

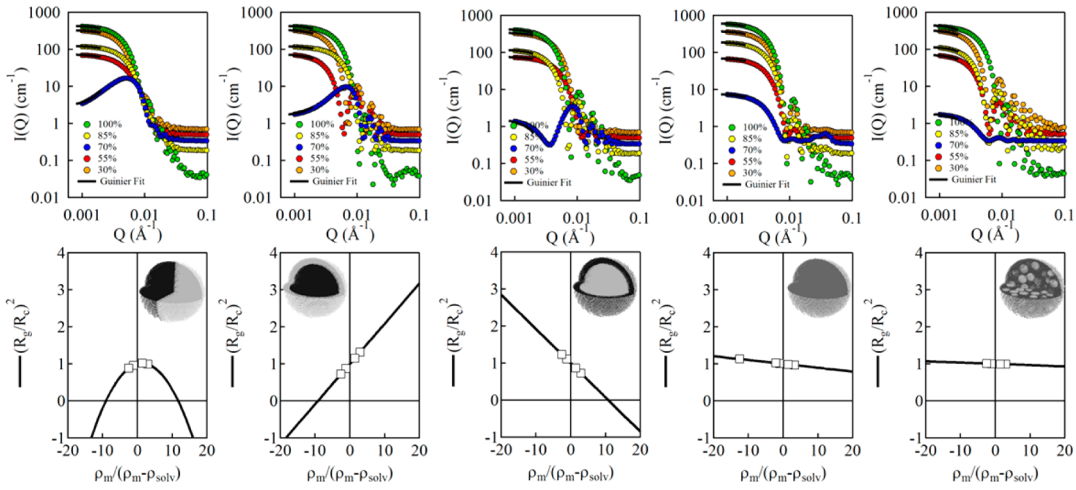

Figure 1. Top: Calculated scattering profiles at five different contrasts for five different shapes: (left to right) eccentric, core−shell (P3HT core), core−shell (PCBM core), uniform, and occluded. Bottom: Corresponding Stuhrmann plots and Monte Carlo lattice representation of the model particles. Gray scale of pixels corresponds to the scattering length density assigned to that pixel with black corresponding to $\rho = 0.0 \times 10^{-6}$ Å^{-2} and white to $\rho = 6.3 \times 10^{-6}$ Å^{-2}. The result of simultaneous Guinier fit is shown as a solid line for each contrast in the top plots.

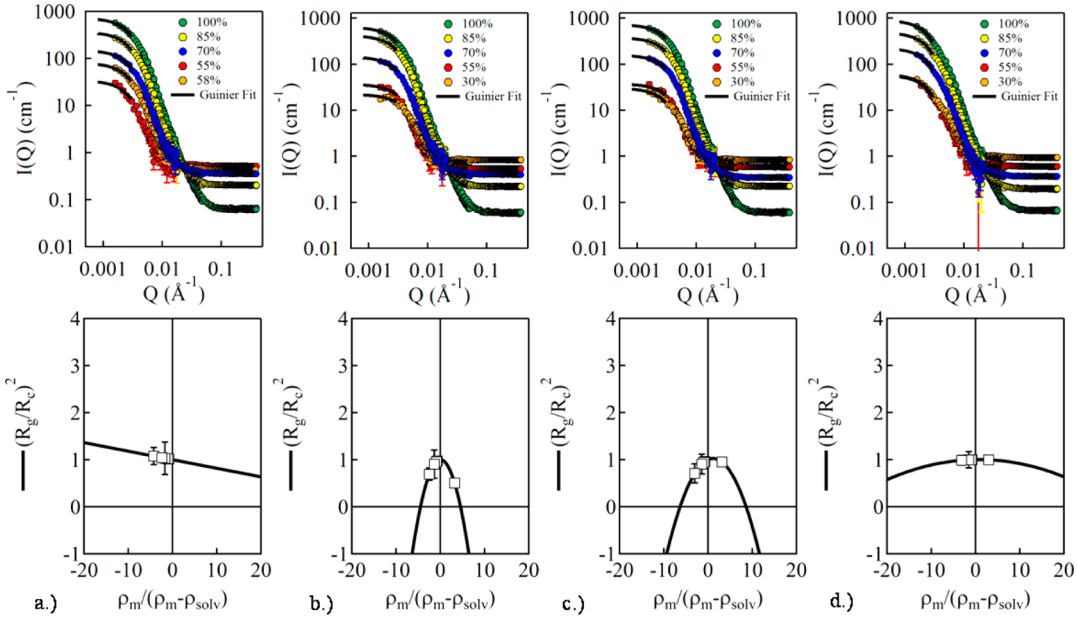

Figure 2. Top: SANS profiles for each sample measured at five unique contrasts and the corresponding Guinier fits (solid line). Bottom: Stuhrmann plots of R_g^2 *vs* $\rho_{part}/\Delta\rho$ for (a) 50/50 P3HT/PCBM latex dispersions, (b) P3HT/$PC_{60}BM/C_{60}$ dispersions, (c) 50/50 P3HT/PCBM postgel, and (d) 50/50 P3HT/PCBM pregel.

core−shell particle where P3HT is enriched in the shell due to the negative α value and $\beta = 0$. This also agrees with the recently published findings using X-ray composition imaging for particles by Ulum *et al.*[15] The sample in Figure 2b is a 1:1 P3HT/fullerene latex where the fullerene phase has 5 wt % C_{60} and 95 wt % PCBM. Previous work on fullerene blend systems has shown that C_{60} nucleates the growth of PCBM aggregates in P3HT/fullerene thin-film composites.[17] We hypothesized that this would also alter the extent of phase segregation within the particle. This particle formulation shows a structure characteristic of eccentric or anisotropic phase segregation based on the quadratic dependence of the Stuhrmann plot. From the results shown in Table 1, β is large and α is also large and positive. This indicates that PCBM is preferentially segregated to the shell of the particle, and that the center of mass of the fullerene phase does not coincide with the center of mass of the particle. The presence of a relatively small amount of C_{60} is shown to have a significant influence over the distribution of PCBM within the particle volume. The samples in Figure 2c,d correspond to the "postgel" and "pregel", respectively. The postgel sample displays a similar

quadratic profile to the P3HT/PCBM/C_{60} latex, suggesting that the particle is eccentric. However, for these particles, there is a smaller β value and a large, negative α value. On average, these particles have an enriched P3HT shell with an eccentric distribution of internal components. As shown in Figure 2d, the pregel sample shows almost complete uniformity because α is zero and β is also very small. Based on our previous work, this indicates that the porous and uniform organogel structure is preserved even when formed in the presence of PCBM.

These results verify that it is possible to form a variety of structures based on the method of nanoparticle preparation. This is not surprising considering the complex behavior shown in P3HT/PCBM thin-film composites.[18−20] Changing the method or the relative composition of materials affects not only photovoltaic performance but also fullerene aggregation from the disordered regions of the P3HT matrix. The specific internal structure directly influences the amount of interface that is available for exciton dissociation and also the percolation of these phases for effective charge transport. Efficient bulk heterojunction structures balance the total available interface for exciton dissociation with the formation of efficient charge transport pathways to the external electrodes. Considering the extension of this insight to a polymer/fullerene SNP, it is likely desirable that domains within the nanoparticle be uniformly distributed and interconnected. The pregel sample is the only dispersion that appears to have a uniform distribution of P3HT and PCBM throughout the nanoparticle's volume. Understanding how particle formulation determines the internal structure is therefore critically important to make SNPs that are likely to yield efficient active layers and devices. To investigate this point further, dispersions of P3HT/PCBM were prepared from chloroform with a fixed size but with varying P3HT/PCBM ratio. The scattering profiles and the Stuhrmann plot for each particle are shown in Figure 3.

As the P3HT content of the particle increases, the value of α also increases, eventually switching from negative to positive (Table 2). This implies that, even in P3HT-deficient particles, PCBM is enriched in the core. Therefore, it appears that PCBM may be preferentially segregated to the core of these composite nanoparticles. For P3HT-rich particles, α is small and β is large,

TABLE 1. Stuhrmann Analysis Results for P3HT/Fullerene SNPs with Variations in Method of Preparation.

	50/50 $CHCl_3$	PCBM/C_{60} $CHCl_3$	toluene postgel	toluene pregel
η_{P3HT} (%)	58	57	58	55
ρ_{part} (Å^{-2})	2.52×10^{-6}	2.57×10^{-6}	2.67×10^{-6}	2.74×10^{-6}
α	−0.016	0.066	−0.066	−0.002
β	1.32×10^{-12}	8.54×10^{-8}	3.20×10^{-8}	2.70×10^{-9}
R_c (nm)	54.2	51.4	49.4	61.5

TABLE 2. Simultaneous Fitting Results from Stuhrmann Analysis for P3HT/PCBM SNPs as a Function of Composition.

	30/70	40/60	50/50	60/40	70/30
η_{P3HT} (%)	36	46	58	66	76
ρ_{part} (Å^{-2})	3.30×10^{-6}	3.39×10^{-6}	2.52×10^{-6}	2.68×10^{-6}	2.27×10^{-6}
α	−0.15	−0.08	−0.02	−0.05	0.05
β	0.00	0.00	1.32×10^{-12}	2.80×10^{-8}	2.30×10^{-8}
R_c (nm)	52.8	57.0	54.2	57.1	57.0

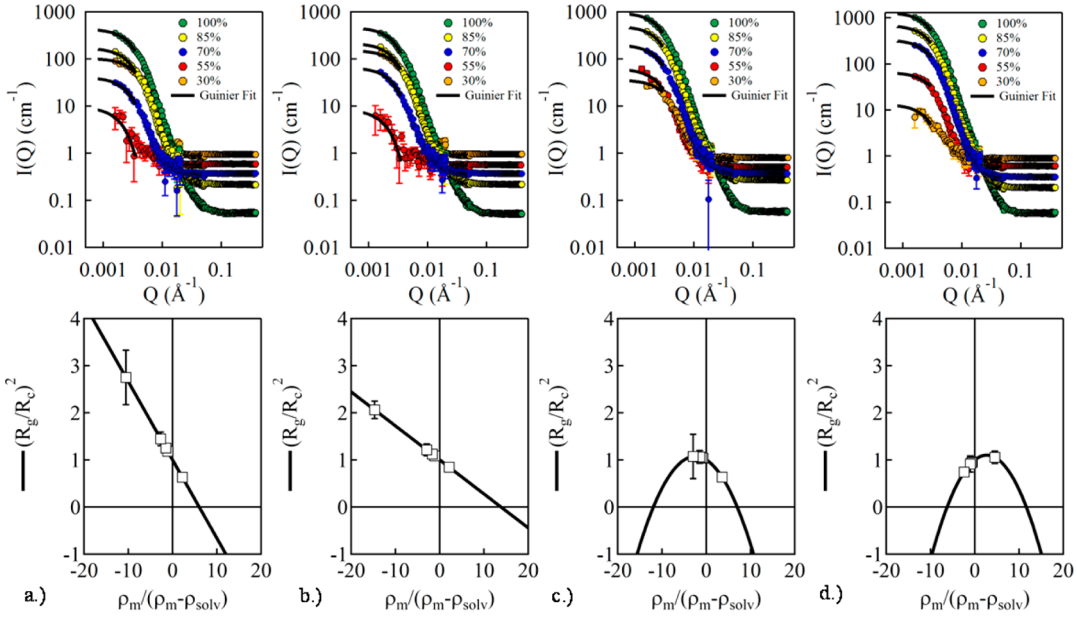

Figure 3. Top: Scattering profiles with corresponding Guinier fits (solid lines) for composite P3HT/PCBM particles created from chloroform as a function of composition for (a) 30/70 P3HT/PCBM, (b) 40/60 P3HT/PCBM, (c) 60/40 P3HT/PCBM, and (d) 70/30 P3HT/PCBM. Bottom: Stuhrmann plot corresponding to each particle.

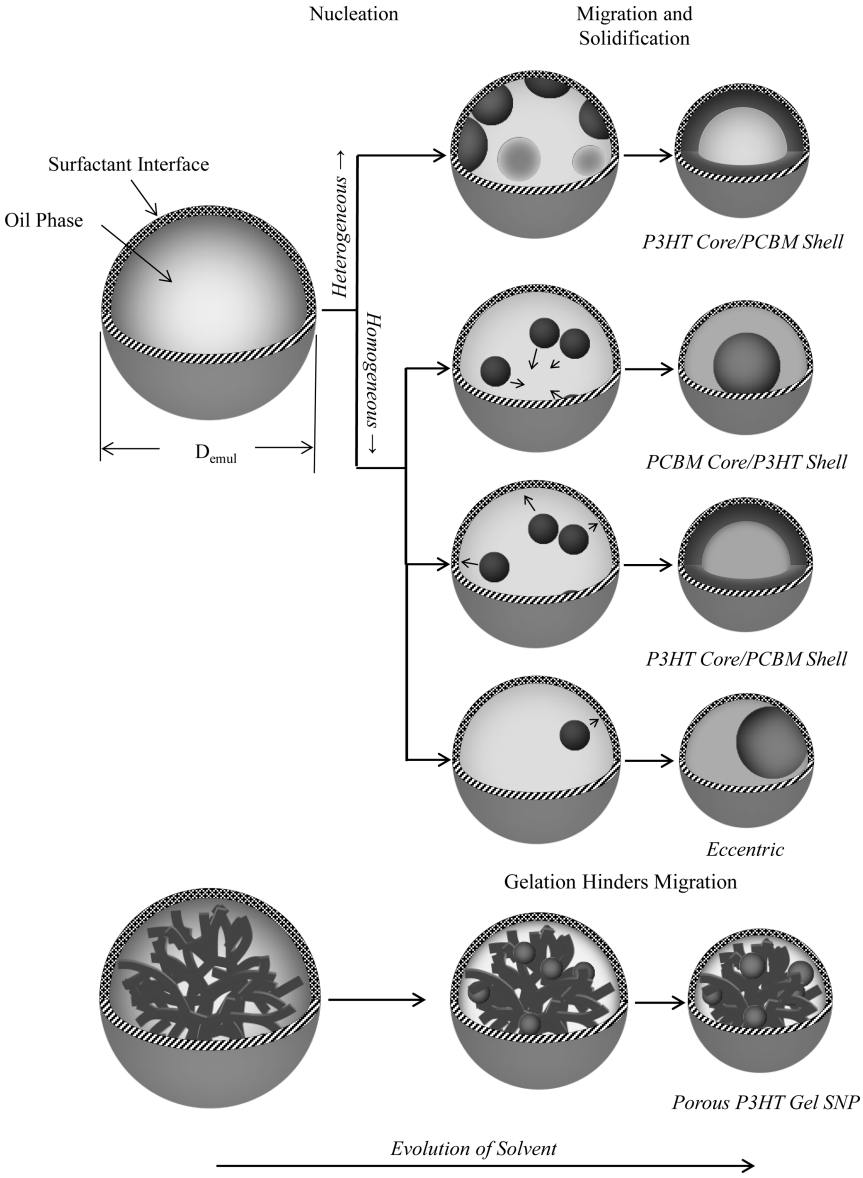

Figure 4. Schematic diagram of the segregation of components internal to an emulsion droplet during the removal of oil. The dark colorized regions are the PCBM-rich phases, and the lighter colors are P3HT-rich phases.

suggesting that these particles are eccentric. Based on this degree of eccentricity, the center of mass of the particle is displaced from its center of scattering length density by ~10% of its radius. The presence of varying amounts of surfactant at the SNP/water interface can account for the slight variations in ρ_{part} from the expected values as a function of composition. Generally, however, the particles show a decrease in ρ_{part} with increasing P3HT content, an expected effect of changing the composition of the SNP.

DISCUSSION

Based on the results presented, it is possible to hypothesize a mechanism for how the specific morphology of SNPs results from any given preparation method. As organic solvent is removed during the evaporation phase of the particle preparation process, soluble components are enriched in the organic solvent. Once supersaturated, nucleation and growth of P3HT and/or PCBM-rich phases can occur. In an emulsion droplet, nucleation could be dominated either by heterogeneous nucleation at the oil/water interface or by homogeneous nucleation in the bulk phase of the emulsion droplet as depicted in Figure 4. If nucleation occurs primarily through a heterogeneous mechanism at the oil/water interface, a shell forms that would, upon full removal of solvent, result in a core–shell particle.[16]

If homogeneous nucleation is dominant, then the relative migration of polymer and fullerene phases within the droplet will determine the ultimate distribution of internal components. The migration of these phases will be determined by the preference of the solvent for the oil/water interface. The removal of solvent from the emulsion phase occurs at the oil/water

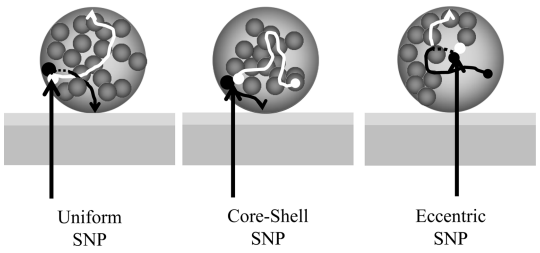

Figure 5. Schematic of exciton diffusion, dissociation, and charge transport through the domains of a SNP as a function of internal morphology.

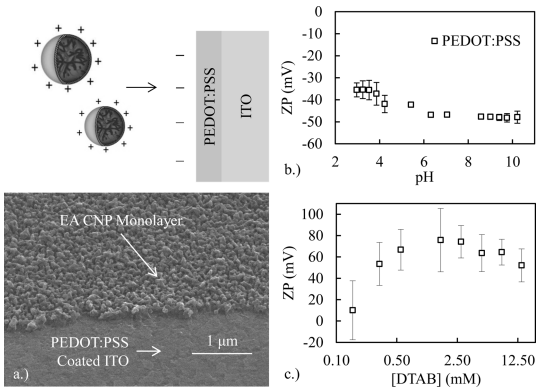

Figure 6. (a) Schematic showing the electrostatic deposition procedure and SEM of dense SNP monolayer film deposited in PEDOT:PSS-coated ITO. (b) Streaming potential measurement of ITO substrate and PEDOT:PSS-coated ITO substrate as a function of pH. (c) Zeta-potential of 60 nm SNP dispersion as a function of DTAB concentration.

interface where it can dissolve into bulk water, be incorporated into the hydrophobic core of micelles in solution, and be brought to the surface of the emulsion and evaporate. The structure of the SNP is therefore determined in part by the rate of diffusion of P3HT and PCBM domains to the core or the shell (depending on affinity) of the emulsion. Since fast solvent removal from drops can effectively arrest these processes, it is unlikely that truly equilibrated structures are forming at all times. This is particularly true for dispersions prepared from chloroform solutions where the typical time for complete removal of solvent is just 5 min. Arrested particle migration caused by rapid solvent removal can account for the formation of eccentric particles. The value of using the P3HT organogel is that gelation of the solution prior to emulsification hinders migration of the internal components during the removal of solvent. Because the P3HT organogel spans the entire volume of the emulsion droplet, the resulting internal components remain uniformly distributed in the resulting SNP. This structure would be somewhat similar to the occluded particle shown in Figure 1.

Based on the structural characterization of SNPs, there are three characteristic structures that can be present, the core–shell particle, eccentric particles, and particles with relatively uniform distribution. It is expected that these particles will exhibit significantly different photovoltaic performance based on their structural features. This is due to the fact that the internal structure will determine the efficiency of exciton dissociation as well as charge transport. As shown in Figure 5, we expect that the best performing SNPs will be those that have uniform distributions of P3HT and PCBM domains. For core–shell particles, there is sufficient interface so that many excitons may be readily dissociated. However, due to the enrichment of one component over the other in the shell, charge transport out of the particle will be hindered. In the case of an eccentric particle, there is likely a lower amount of interface available for exciton dissociation, and the ability of charges to reach electrodes will depend on the specific orientation of the particles relative to the electron and hole transport layers that are present in typical device geometries. Therefore, misalignment of the electron or hole conducting domains with electron and hole buffer layers will lead to inefficient carrier extraction. A uniform distribution of material in the particle volume ensures that there is both sufficient interface for excitons to dissociate and a clear pathway for transport of charges out of the interior domains of a SNP.

In order to validate this hypothesis, it is necessary to evaluate the intrinsic charge generation properties of different particle formulations while eliminating the possible convolution of these results from processes that are extrinsic to the particles (*e.g.*, particle–particle charge transport in multilayers). To do this, it is first necessary to generate a uniform monolayer of particles so that factors like interparticle transport and nonuniform illumination do not influence the measurement. In order to coat monolayers, we developed a novel electrostatic deposition (ED) technique. Using positively charged (cationic) SNP dispersions, it is possible to electrostatically assemble monolayers of SNPs onto a negatively charged PEDOT:PSS film, as shown in Figure 6a. The methodology is relatively simple. The surface charge of the surface that is to be coated is determined as a function of pH *via* streaming potential measurements (Figure 6b). Based on these measurements, PEDOT:PSS always has a strong negative charge regardless of the pH. For negative surfaces (*e.g.*, PEDOT:PSS) and positive particles (DTAB-stabilized dispersions), the pH and the bulk concentration of DTAB are tuned such that both particles and surface have large opposite surface charges and also such that there is as little "free" surfactant as possible while maintaining colloidal stability. In this case, a neutral pH was chosen. The reduction of free DTAB minimizes the competitive adsorption of surfactant on the PEDOT:PSS film and ensures the formation of dense particle monolayers over the PEDOT:PSS surface. The optimum concentration of surfactant was found by measuring the ζ-potential of the particles as a function

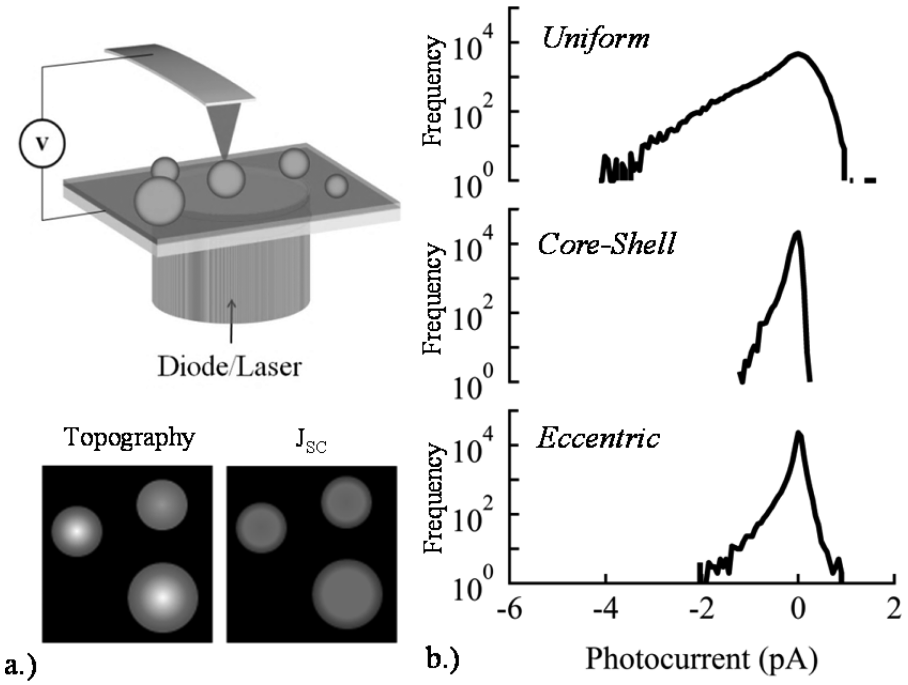

Figure 7. (a) Schematic of pcAFM experiment and (b) histograms of photocurrent produced from monolayer films of uniform, core–shell, and eccentric particles. The particles all have the same overall composition and correspond to the toluene pregel, P3HT/PCBM from chloroform, and P3HT/PCBM/C_{60} from chloroform, respectively.

of DTAB concentration (Figure 6c). At a concentration of around 2 mM DTAB, the ζ-potential of the SNPs began to decrease, suggesting desorption of surfactant from the SNP/water interface. This is the point where the chemical potential of adsorption of DTAB to the SNP surface matches that of the bulk solubility of DTAB. Reducing the bulk DTAB concentration too much reduces the particle charge and, eventually, will also lead to particle aggregation and flocculation. Nevertheless, we find that the best coating conditions are found when the surfactant concentration is less than 2 mM and the ζ-potential is still greater than 30 mV. At this point, the dispersion is still colloidally stable and positively charged, but there is very little free DTAB to compete for the surface. ITO films coated with PEDOT:PSS are shown to readily form dense monolayers of SNPs after just 30 min of exposure to dispersions containing 0.1 vol % SNPs and 0.5 mM DTAB.

In order to characterize the intrinsic charge generation properties of individual nanoparticles with different formulations and morphologies, photoconductive AFM (pcAFM) measurements were performed on electrostatically deposited films of pregel, eccentric, and core–shell SNPs with identical P3HT/fullerene ratio. Using pcAFM, it is possible to individually measure the photocurrent from a monolayer of nanoparticles. In this way, it is possible to isolate the intrinsic carrier generation and transport properties within individual nanoparticles without any influence from extrinsic device properties. While these measurements cannot necessarily be used at this time to fully predict the performance of devices processed from SNPs, they are a direct probe of the intrinsic nanoparticle photocurrent generation. In a pcAFM measurement, an electrically conductive tip, in this case gold, is placed in direct contact with the nanoparticle surface so that the electronic circuit is completed with the underlying conductive substrate, as shown in Figure 7a. Monochromatic light (λ = 532 nm) is then used to illuminate the particles, and as the tip scans over the surface, the tip voltage is maintained at zero as it raster scans over the sample surface. PcAFM in Figure 7 was performed at the short circuit condition (0 V bias), so the charges harvested at the gold AFM tip directly correspond to spontaneous current generation originating within each nanoparticle. Depending on the composition of the nanoparticle and region of it that is in contact with the AFM probe (be it fullerene-rich or polymer-rich), electrons or holes will preferentially enter the tip, leading to positive or negative currents. Therefore, pcAFM experiments measure the performance of many isolated nanoparticles that act as individual nanosized solar cells. At the same time that photocurrent information is obtained, pcAFM also acquires a topological image that provides a means to correlate the particle position and size to the photocurrent. For the images acquired, the resolution is 15 nm/pixel so that differences in nanoscale photocurrent generation can be differentiated.

Photocurrent images were taken for each nanoparticle formulation, and representative histograms are shown in Figure 7b. Based on these results, it is clear that the pregel particle has the best single-particle performance when compared to the

core−shell or eccentric particles. This is indicated by the significantly larger hole (up to 4 pA) and electron currents (~1 pA) that are consistently observed for films produced from these particles. The core−shell particle showed moderate hole current with maximum values of ~1 pA but almost no electron current, whereas the eccentric particle showed larger hole currents (up to 2 pA) than the core−shell particle but also higher electron currents (<1 pA). These results support the proposed structural models for these particles. The core−shell particle has a P3HT-rich shell, and therefore, it is more difficult for photogenerated electrons to be transported out of the particle, leading to higher rates of internal recombination and subsequently lower measured photocurrents. The eccentric particle showed moderate hole and electron currents, which is consistent with orientation dependence of electron and hole current generation. Finally, the pregel particles that were prepared using the organogel porous framework showed the best performance because of the uniform distribution of both semiconductor materials within the SNP. This ensures that there is a large amount of p/n junction interface for exciton dissociation and that the rate of hole and electron transport out of the SNP is also effective because there is no preferential enrichment of one material over the other at the particle's surface.

CONCLUSIONS

In this work, we prepared and analyzed eight different composite nanoparticles, four with similar composition but variable formulation strategy and four other SNP having a fixed preparation method and variable composition. Contrast variation small-angle neutron scattering was used to probe the internal structure of these particles as a function of these variables. We also used MC sampling to calculate scattering patterns of several model nanoparticle systems having variable internal structure and material distribution. Stuhrmann plots generated from the simulated structures were used as a basis of comparison for those of real SNPs. In doing so, the structural characteristic of each nanoparticle formulation was identified and discussed. We then proposed a model to describe the physical processes that lead to a diverse range of internal morphologies for SNPs. Finally, we used pcAFM as a probe of photocurrent generated from monolayer films prepared from different methods using electrostatic deposition. From these results, it was possible to correlate intrinsic performance characteristics with the specific structure of the particles.

This work demonstrates that there is a great diversity of structural morphology that is achievable in SNPs as a function of small changes in formulation. This work also highlights the importance of having a systematic method to characterize and quantify the morphology of polymer/fullerene SNPs for use in photovoltaic applications. While it is clear that the specific structural morphology of a SNP is not the only factor that will ultimately determine device performance, the intrinsic charge generation and transport properties of SNPs does limit the maximum achievable performance within any composite film that is prepared from these particles. Thus, we conclude that it is critical to first optimize the intrinsic properties of SNPs before attempting to optimize the extrinsic properties that are controlled *via* film deposition methods, device engineering, or other design processes. Work related to the fabrication of functional photovoltaic devices from monolayer films of SNPs is ongoing and will be the subject of a future publication.

METHODS

General Preparation of Nanoparticle Dispersions. The poly(3-hexylthiophene) was Sepiolid P100 grade purchased from Rieke Metals (Lincoln, NE). The [6,6]phenyl-C_{60}-butyric acid methyl ester was purchased from SES Research (Houston, TX). The deuterated sodium dodecyl sulfate (d-SDS) was used as received from CDN isotopes (Quebec, Canada). P3HT/PCBM particle dispersions were produced by dissolving known amounts of P3HT and PCBM into organic solvent. For P3HT/PCBM nanoparticles produced from chloroform and toluene, the volume fraction of total solids was held constant at 3.1%. This organic phase was added to 40 mM d-SDS dissolved in D_2O in a 1:10 o/w ratio and using a Branson Sonifier 450, emulsified at 70% intensity for 15 s, using 1 s pulses with a 1 s delay between pulses. The resulting stable emulsion was placed in a 10 mL round-bottom flask and stirred under vacuum at room temperature to remove the organic solvent from the emulsion.[11,21] This process resulted in stable composite nanoparticles containing the desired ratio of P3HT/PCBM. For this work, we created dispersions with a concentration of 2.5 vol % total solids, and the method usually resulted in composite nanoparticles with an average hydrodynamic radius of 65 nm as measured using dynamic light scattering (Malvern Zetasizer). The exact concentration of solids in the solution was also corroborated using thermogravimetric analysis with a TA Q50 after the final dispersions were prepared. The P3HT volume percent, η_{P3HT}, of the dispersed nanoparticles was also verified again after preparation by redissolving a dry dispersion in a good solvent (*i.e.*, chloroform). The absorption spectra of redissolved samples were measured again, and using known extinction coefficients ($\varepsilon_{P3HT} = 53.2$ mL/(mg·cm), $\lambda = 462$ nm; $\varepsilon_{PCBM} = 60.8$ mL/(mg·cm), $\lambda = 330$ nm; $\varepsilon_{C60} = 90.0$, $\lambda = 333$ nm), we determined the total content of each component in the particles. There was generally very good agreement between formulation and the resulting compositions. For the SANS measurements, all dispersions were diluted to the same total P3HT/PCBM solids content (ϕ = 0.25 vol %). The excess d-SDS that is needed for efficient emulsification was removed by dialysis with a solution of 5 mM d-SDS (below the CMC) that did not reduce colloidal stability. Samples with identical composition but with five different neutron scattering contrast values in the solvent were then prepared by diluting these stock dispersions into solutions of varying H_2O/D_2O content. Small-angle neutron scattering experiments were then carried out in the NG3 beam line at NCNR in Gaithersburg, Maryland. Samples were measured at a sample-to-detector distance of 13 m using lenses and wavelength λ = 8.5 Å, as well as at 6 and 1 m configurations with λ = 6 Å.[22] The counting time at each position was varied

according to the contrast of the solvent and the particles to achieve adequate statistics. Sample transmission was measured at the largest sample-to-detector distance for each wavelength, and beam flux measurements were used to convert the scattering profiles to an absolute scale.

Variations in Formulation Methods for Nanoparticle Dispersions. There are two unique SNP preparation strategies used in this work. The first is the method outlined by Landfester for the preparation of SNPs from chloroform, which is a good solvent for both components. In this method, the removal of solvent is the primary driver for structural development within the nanoparticle. The second strategy for nanoparticle formulation is to use polymer gelation as a means to control the nanoparticle structure. The preparation of P3HT organogels has been outlined previously, but it is briefly reviewed here.[23,24] A P3HT organogel in toluene is prepared by heating a P3HT solution to 80 °C, where the polymer is fully soluble, followed by cooling the solution to room temperature. Because the solubility of P3HT in toluene is moderate and temperature-dependent (~3 mg/mL at 25 °C), solutions become supersaturated at lower temperatures and P3HT self-assembles into nanofibrillar aggregates that form a physical gel. The strength and conductivity of P3HT gels are concentration-dependent and solvent-dependent.[25] Here toluene was used as the solvent because it has a relatively high solubility for PCBM (6 mg/mL), and it is also modestly soluble in water so that solvent extraction is facilitated. In this method, a porous P3HT organogel can be formed and the void volume can be filled with PCBM or other n-type semiconductors. Two different variations in this method were used to make the composite gel dispersions characterized in this work. In the first approach, termed "pregel", emulsification was carried out after the polymer solution had been allowed to form a gel at room temperature for a full day in the vial. In this method, a macroscopic gel fully develops in a vial and it is subsequently fractured into smaller dispersed particles in the presence of water and surfactant. For P3HT organogels, this procedure results in porous P3HT particles that are filled with toluene.[26] The second approach yields particles that are termed "postgel" dispersions. In these samples, emulsification proceeded immediately after cooling the toluene solution to room temperature, and the dispersion was allowed to develop for 24 h at room temperature before the solvent was removed. In this way, the soluble P3HT slowly crystallizes within the confined space of the emulsion droplet while PCBM remains soluble.

SANS Data Analysis. Contrast variation is used to characterize the internal structure of composite nanoparticles.[27] By measuring the same sample in solutions with varying amounts of H_2O and D_2O, Stuhrmann demonstrated that the dependence of scattering intensity for any inhomogeneous particle can be decomposed into separate terms as shown in eq 1.[28−30]

$$I(Q, \Delta\rho) = I_{IH}(Q) + \Delta\rho \times I_{cs}(Q) + (\Delta\rho)^2 \times I_H(Q) \quad (1)$$

where $\Delta\rho = (\rho_m - \rho_{solv})$.

For homogeneous particles without internal inhomogeneities, $I(Q)$ is the product of the form factor $P(Q)$ and the structure factor $S(Q)$. In most cases, measurements are made in dilute solution to minimize interactions between particles so that $S(Q) = 1$ and the scattering profile is dominated by $P(Q)$.[31,32] A large number of analytical form factor models for homogeneous particles exist to predict the scattering profile.[33−35] For inhomogenous particles, the scattering profile is a function of the overall particle's shape, $I_H(Q)$, the shape function of its inhomogeneities, $I_{IH}(Q)$, and a structural correlation term, $I_{cs}(Q)$. Taken together, these functions reconstruct the scattering from the entire particle.

In this description, the scattering from an object with average scattering length density, ρ_m, has a quadratic dependence on contrast between the object and its solvent, $\Delta\rho$. By measuring the sample in at least three different solvent contrasts, the terms in eq 1 can be fit at every Q value to the known contrast term and the constituent basis functions ($I_H(Q)$, $I_{IH}(Q)$, $I_{cs}(Q)$) of the shape can be recovered. In principle, the form factor of the object is thus separated from the form factor of the inhomogeneities, and the basis functions can now be fit independently using analytical models for homogeneous particles. Despite the power of this description, for samples that have polydispersity in both size and shape, it often proves difficult to identify adequate analytical models for the basis functions, and the resolution of measurements particularly at high Q, where incoherent scattering is dominant, is insufficient to measure the inhomogeneous term accurately. For samples whose basis functions cannot be reconstructed or where fits with analytical form factor models are poor, Stuhrmann derived eq 2 to describe the quadratic dependence of R_g of a particle on the inverse of the $\Delta\rho$.

$$R_g^2 = R_c^2 + \frac{\alpha}{\Delta\rho} - \frac{\beta}{\Delta\rho^2} \quad (2)$$

In eq 2, R_c is the radius of gyration of the particle at infinite contrast (*i.e.*, if it were homogeneous), α describes the relative distribution of scattering length density radially from the particle's center of mass, and β is the measure of distance of the center of mass of the particle to the center of mass of its heterogeneous components. In effect, the overall shape of the particle is described by R_c and the distribution of inhomogeneities by α and β. The result of this analysis showed that a plot of R_g^2 as a function of $1/\Delta\rho$ is a unique fingerprint that can be used to identify materials by their average distribution of internal inhomogeneities.[28]

Using Stuhrmann analysis, the internal structure of SNP is assigned specific structures based on model predictions. In order to gain physical insight into the expected shape of the Stuhrmann plot for several plausible nanoparticle structures, possible hypothetical structures were constructed and the scattering was calculated in absolute scale units using Monte Carlo sampling (Supporting Information Figure S.4). The simulated composite nanoparticles have R = 50 nm, and they explicitly include a 1.5 nm layer of d-SDS ($\rho_{d\text{-}SDS} = 6.1 \times 10^{-6}$ Å^{-2}) with pure domains of P3HT ($\rho_{P3HT} = 0.7 \times 10^{-6}$ Å^{-2}) and PCBM ($\rho_{PCBM} = 4.4 \times 10^{-6}$ Å^{-2}). Several different structures, which are all possibilities in the experimental system, are modeled based on the fixed P3HT/PCBM mass ratio. Guinier fits of the simulated and the experimental SANS data are used to extract R_g and $I(0)$ for each particle formulation at all solvent contrast values. Using the known solvent scattering length density, the Stuhrmann plots are then constructed and fit to a quadratic function to extract α and β values as outlined in the Supporting Information. While it is not shown, there is linear dependence of the $I^{1/2}(0)$ *versus* ρ_{solv} for all of these particles, demonstrating that the scattering is derived from a single scattering entity with a characteristic ρ_{part} and not from a mixture of two discrete particle populations. The Stuhrmann analysis is also shown to be valid for particles that have some polydispersity in both size or in internal composition (Figure S.6). The resulting Stuhrmann plots for polydisperse samples represent an average over the entire particle distribution. Despite being relatively robust, this method does break down for very large values of polydispersity (PDI > 0.5). Yet, based on DLS and SEM measurements of the particles used for SANS measurements, the size distributions are sufficiently narrow for the approach to remain valid (Figures S.2 and S.3).

Electrostatic Assembly of SNP Monolayers. For SNP prepared using SDS, the stabilizing agent was subsequently exchanged with dodecyl trimethylammonium bromide (DTAB) (Aldrich, St. Louis, 99.9% reagent grade) to produce cationic particles. This exchange was performed by extensive dialysis that was also monitored with ζ-potential measurements using a Zetasizer Nano with a reusable dip cell. To exchange surfactant, the dispersion's surfactant concentration was first reduced from 40 to 1 mM SDS, and then ultrafiltration was used to fully exchange the remaining SDS with a 40 mM DTAB solution using 100 kDa Millipore filter. A number of washes were performed to ensure complete removal of SDS. The resulting DTAB-stabilized dispersion was then dialyzed to a concentration of 5 mM DTAB to remove free surfactant. This stock nanoparticle solution was further diluted to a final concentration of 0.5 mM DTAB and 0.1 vol % SNPs. Spin-coated PEDOT:PSS (Clevios AI 4083) films (3500 rpm for 1 min) on 15 mm × 15 mm ITO substrates were

prepared and baked at 140 °C for 30 min. These films were then extensively washed with DI water to remove excess PSS. The films were then dipped into the SNP coating solution for 30 min, where electrostatic attraction between the cationic nanoparticles and the anionic PEDOT:PSS film resulted in monolayer adsorption. The films were rinsed with copious amounts of DI water to remove excess particles and dried under nitrogen and vacuum for 1 day.

Photoconductive AFM. Photoconductive atomic force microscopy was carried out on an Asylum Research MFP-3D BIO system. Gold-coated contact mode AFM tips with a force constant of 0.2 N/m (Budget Sensors, Cone-GB) were used for all experiments. A 532 nm wavelength illumination with an intensity of 218 W/cm^2 was used prior to entering the microscope optics and aligned directly under the AFM tip. The tip−sample contact force was kept to a minimum, typically ~10 nN to avoid damaging the film. No external voltage bias was applied to the AFM tip.[36]

Conflict of Interest: The authors declare no competing financial interest.

Acknowledgment. The authors principally acknowledge funding from the Department of Energy Office of Basic Energy Sciences for financial support of this work under Grant Nos. DE-SC0005153 and DE-SC0010282. This work benefitted from SASView software, originally developed by the DANSE project under NSF Award DMR-0520547. This work utilized facilities supported in part by the National Science Foundation under Agreement No. DMR-0944772. We acknowledge the support of the National Institute of Standards and Technology, U.S. Department of Commerce, in providing the neutron research facilities used in this work. The authors would also like to thank Vinod Radhakrishnan for his assistance in measuring streaming potential using the Anton Paar Surpass instrument. During the time these experiments were conducted, G.S. received partial support by NSF DMR 1306079. We are grateful to Prof. D.S. Ginger for discussions about the initial experiments, and for the use of his atomic force microscopes, purchased with support from AFOSR.

Supporting Information Available: The IGOR Pro routine and documentation for calculation of scattering profiles in absolute scale as a function of solvent contrast is available upon request. Supplemental figures. This material is available free of charge *via* the Internet at http://pubs.acs.org.

REFERENCES AND NOTES

1. Dennler, G.; Scharber, M. C.; Brabec, C. J. Polymer-Fullerene Bulk-Heterojunction Solar Cells. *Adv. Mater.* **2009**, *21*, 1323–1338.
2. Moulé, A. J.; Meerholz, K. Morphology Control in Solution-Processed Bulk-Heterojunction Solar Cell Mixtures. *Adv. Funct. Mater.* **2009**, *19*, 3028–3036.
3. Hoppe, H.; Sariciftci, N. S. Morphology of Polymer/Fullerene Bulk Heterojunction Solar Cells. *J. Mater. Chem.* **2006**, *16*, 45–61.
4. Hwang, I.; Moses, D.; Heeger, A. J. Photoinduced Carrier Generation in P3HT/PCBM Bulk Heterojunction Materials. *J. Phys. Chem. C* **2008**, *17*, 4350–4354.
5. Pearson, A. J.; Wang, T.; Lidzey, D. G. The Role of Dynamic Measurements in Correlating Structure with Optoelectronic Properties in Polymer: Fullerene Bulk-Heterojunction Solar Cells. *Rep. Prog. Phys.* **2013**, *76*, 022501–022517.
6. Landfester, B. K.; Montenegro, R.; Scherf, U.; Güntner, R.; Asawapirom, U.; Patil, S.; Neher, D.; Kietzke, T. Semiconducting Polymer Nanospheres in Aqueous Dispersion Prepared By a Miniemulsion Process. *Adv. Mater.* **2002**, *14*, 651–655.
7. Andersen, T. R.; Larsen-Olsen, T. T.; Andreasen, B.; Böttiger, A. P. L.; Carlé, J. E.; Helgesen, M.; Bundgaard, E.; Norrman, K.; Andreasen, J. W.; Jørgensen, M.; *et al.* Aqueous Processing of Low-Band-Gap Polymer Solar Cells Using Roll-to-Roll Methods. *ACS Nano* **2011**, *5*, 4188–4196.
8. Kietzke, T. Nanostructured Solar Cells Based on Semiconducting Polymer Nanospheres (SPNs) of M3EH-PPV and CN-Ether-PPV. *Proc. SPIE* **2004**, *5215*, 206–210.
9. Holmes, N. P.; Burke, K. B.; Sista, P.; Barr, M.; Magurudeniya, H. D.; Stefan, M. C.; Kilcoyne, A. L. D.; Zhou, X.; Dastoor, P. C.; Belcher, W. J. Nano-Domain Behaviour in P3HT:PCBM Nanoparticles, Relating Material Properties to Morphological Changes. *Sol. Energy Mater. Sol. Cells* **2013**, *117*, 437–445.
10. Hoppe, H.; Sariciftci, N. S. Organic Solar Cells: An Overview. *J. Mater. Res.* **2011**, *19*, 1924–1945.
11. Landfester, B. K.; Montenegro, R.; Scherf, U.; Güntner, R.; Asawapirom, U.; Patil, S.; Neher, D.; Kietzke, T. Semiconducting Polymer Nanospheres in Aqueous Dispersion Prepared by a Miniemulsion Process. *Adv. Mater.* **2002**, *14*, 651–655.
12. Hjelm, R. P.; Wampler, W.; Seeger, P. A.; Gerspacher, M. The Microstructure and Morphology of Carbon Black: A Study Using Small Angle Neutron Scattering and Contrast Variation. *J. Mater. Res.* **1994**, *9*, 3210–3222.
13. Mang, J. T.; Hjelm, R. P.; Orler, E. B.; Wrobleski, D. A. Small-Angle Neutron Scattering of a Solvent-Swollen Segmented Polyurethane as a Probe of Solvent Distribution and Polymer Domain Composition. *Macromolecules* **2008**, *41*, 4358–4370.
14. Pedersen, J. S. Structure Factors Effects in Small-Angle Scattering from Block Copolymer Micelles and Star Polymers. *J. Chem. Phys.* **2001**, *114*, 2839–2846.
15. Ulum, S.; Holmes, N.; Darwis, D.; Burke, K.; Kilcoyne, A. L. D.; Zhou, X.; Belcher, W.; Dastoor, P. Determining the Structural Motif of P3HT:PCBM Nanoparticulate Organic Photovoltaic Devices. *Sol. Energy Mater. Sol. Cells* **2013**, *110*, 43–48.
16. Loxley, A.; Vincent, B. Preparation of Poly(methylmethacrylate) Microcapsules with Liquid Cores. *J. Colloid Interface Sci.* **1998**, *208*, 49–62.
17. Richards, J. J.; Rice, A. H.; Nelson, R. D.; Kim, F. S.; Jenekhe, S. A.; Luscombe, C. K.; Pozzo, D. C. Modification of PCBM Crystallization *via* Incorporation of C60 in Polymer/Fullerene Solar Cells. *Adv. Funct. Mater.* **2013**, *23*, 514–522.
18. Dang, M. T.; Hirsch, L.; Wantz, G. P3HT:PCBM, Best Seller in Polymer Photovoltaic Research. *Adv. Mater.* **2011**, *23*, 3597–3602.
19. Zhao, J.; Swinnen, A.; Assche, G.; Van Manca, J.; Vanderzande, D.; Van Mele, B. Phase Diagram of P3HT/PCBM Blends and Its Implication for the Stability of Morphology. *J. Phys. Chem. B* **2009**, *113*, 1587–1591.
20. Müller, C.; Ferenczi, T. A. M.; Campoy-Quiles, M.; Frost, J. M.; Bradley, D. D. C.; Smith, P.; Stingelin-Stutzmann, N.; Nelson, J. Binary Organic Photovoltaic Blends: A Simple Rationale for Optimum Compositions. *Adv. Mater.* **2008**, *20*, 3510–3515.
21. Landfester, K. The Generation of Nanoparticles in Miniemulsions. *Adv. Mater.* **2001**, *13*, 765–768.
22. Glinka, C. J.; Barker, J. G.; Hammouda, B.; Krueger, S. The 30 m Small-Angle Neutron Scattering Instruments at the National Institute of Standards and Technology. *J. Appl. Crystallogr.* **1998**, *31*, 430–445.
23. Malik, S.; Nandi, A. K. Influence of Alkyl Chain Length on the Gelation Mechanism of Thermoreversible Gels of Regioregular Poly(3-alkyl thiophenes) in Xylene. *J. Appl. Polym. Sci.* **2006**, *103*, 2528–2537.
24. Koppe, M.; Brabec, C. J.; Heiml, S.; Schausberger, A.; Duffy, W.; Heeney, M.; McCulloch, I. Influence of Molecular Weight Distribution on the Gelation of P3HT and Its Impact on the Photovoltaic Performance. *Macromolecules* **2009**, *42*, 4661–4666.
25. Newbloom, G. M.; Weigandt, K. M.; Pozzo, D. C. Electrical, Mechanical, and Structural Characterization of Self-Assembly in Poly(3-hexylthiophene) Organogel Networks. *Macromolecules* **2012**, *45*, 3452–3462.
26. Richards, J. J.; Weigandt, K. M.; Pozzo, D. C. Aqueous Dispersions of Colloidal Poly(3-hexylthiophene) Gel Particles with High Internal Porosity. *J. Colloid Interface Sci.* **2011**, *364*, 341–350.

27. Feigin, L. A.; Svergun, D. I. *Structure Analysis by Small-Angle X-ray Scattering and Neutron Scattering*; Plenum Press: New York, 1987.
28. Stuhrmann, H. B.; Miller, A. Small-Angle Scattering of Biological Structures. *J. Appl. Crystallogr.* **1978**, *11*, 325–345.
29. Stuhrmann, H. B. Neutron Small-Angle Scattering of Biological Macromolecules in Solution. *J. Appl. Crystallogr.* **1974**, *7*, 173–178.
30. Hjelm, R. P.; Wampler, W. The Structure of Carbon Black and Its Associations in Elastomer Composites: A Study Using Neutron Scattering. *Raw Mater. Appl.* **2000**, *53*, 592–595.
31. Lindner, P.; Zemb, T. *Neutrons, X-rays and Light: Scattering Methods Applied to Soft Condensed Matter*; Elsevier: Amsterdam, 2002.
32. Glatter, O.; Kratky, O. *Small Angle X-ray Scattering*; Academic Press Inc.: New York, 1982.
33. Kline, S. R. Reduction and Analysis of SANS and USANS Data Using IGOR Pro. *J. Appl. Crystallogr.* **2006**, *39*, 895–900.
34. *SasView*, http://www.sasview.org/.
35. Tjioe, E.; Heller, W. T. ORNL_SAS: Software for Calculation of Small-Angle Scattering Intensities of Proteins and Protein Complexes. *J. Appl. Crystallogr.* **2007**, *40*, 782–785.
36. Coffey, D. C.; Reid, O. G.; Rodovsky, D. B.; Bartholomew, G. P.; Ginger, D. S. Mapping Local Photocurrents in Polymer/Fullerene Solar Cells with Photoconductive Atomic Force Microscopy. *Nano Lett.* **2007**, *7*, 738–744.